Geophysical Journal International

Geophys. J. Int. (2016) **204,** 167–179
GJI Seismology

doi: 10.1093/gji/ggv420

Crustal structure and deformation beneath the NE margin of the Tibetan plateau constrained by teleseismic receiver function data

Qiong Wang,[1,2,3] Fenglin Niu,[3,4] Yuan Gao[2] and Yuntai Chen[1]

[1] *Institute of Geophysics, China Earthquake Administration, Beijing, China*
[2] *Institute of Earthquake Science, China Earthquake Administration, Beijing, China, E-mail: gaoyuan@seis.ac.cn*
[3] *Department of Earth Science, Rice University, Houston, TX, USA*
[4] *State Key Laboratory of Petroleum Resource and Prospecting, and Unconventional Natural Gas Institute, China University of Petroleum at Beijing, Beijing, China*

Accepted 2015 September 28. Received 2015 September 25; in original form 2015 April 7

SUMMARY

We analysed a large amount of teleseismic receiver function data recorded by 172 broadband stations in the NE Tibetan plateau and its surrounding areas to investigate the crustal velocity and anisotropy structure beneath the margin. We first applied the modified H–κ stacking technique to measure the crustal thickness and average Vp/Vs ratio, and then employed a joint inversion scheme to measure azimuthal anisotropy of the crust beneath each station. The observed crustal thickness and Vp/Vs ratio exhibit large variations across the study area, varying from 32 to 75.6 km and from 1.601 to 1.864, respectively. We also found significant azimuthal anisotropy within the crust beneath 12 stations, with a splitting time between 0.36 and 1.06s. The fast polarization directions align well with surface structures, and follow the directions of the maximum horizontal tensile stress. The low Vp/Vs ratio and the strong azimuthal anisotropy observed beneath the margin suggest that whole crustal shortening might be the dominant mechanism for producing the thick crust in NE Tibet. We compared the measured seismic anisotropy with those measured from XKS (SKS, PKS and SKKS), and found that crustal anisotropy appears to play an important role in explaining the amount of XKS splitting times. More importantly, the Moho Ps and the XKS share similar fast polarization directions, suggesting a vertically coherent deformation within the lithosphere beneath the margin.

Key words: Seismicity and tectonic; Body waves; Seismic anisotropy; Crustal structure; Asia.

1 INTRODUCTION

Mountain building and plateau forming are fundamental tectonic processes that have not been fully understood yet. The NE Tibetan plateau is one of the best places on the globe to study these processes because of the pervasive active overthrusting across this corner of the plateau. Geographically, the NE Tibet plateau is limited by two NWW–SEE trending thrust belts: the Qilian thrust belt in the north and the Eastern Kunlun transpressional system in the south (Fig. 1). The Haiyuan fault and the Altyn Tagh fault define its northeast and northwest boundaries, respectively (Tapponnier *et al.* 2001). As the northern boundary of the Tibetan plateau, the Qilian orogen, which was developed at the southern margin of the North China craton before it was offset by the Altyn Tagh fault in the Cenozoic, consists of complexly deformed early Palaeozoic arcs (Yin & Harrison 2000), and is undergoing ∼NNE–SSW horizontal shortening at a rate of about 12 mm yr^{-1} (Zhang *et al.* 2004). The eastern Kunlun-Qaidam terrane in the south is comprised of a broad early Palaeozoic arc and a younger and narrower late Permian to Triassic arc (Yin & Harrison 2000). The Songpan-Ganzi block, to the south of the eastern Kunlun fault, was an accretionary prism formed during the northward subduction of the oceanic Qiangtang lithosphere beneath the Tarim-North China block (Watson *et al.* 1987).

The large-scale surface deformation, uplifting and faulting occurring in the NE Tibet are generally believed to be caused by the continuous collision between the India and Eurasia since ∼50 Myr (Molnar & Tapponnier 1975; Yin & Harrison 2000). However, the style and amount of the subsurface deformation driven by the collision, especially those inside the lower crust and upper mantle, are still debated. Many models have been proposed to explain the deformation of the Tibetan Plateau, such as uniform lithospheric shortening (e.g. England and Houseman 1986; Dewey *et al.* 1988) and crustal channel flow (Clark & Royden 2002). The first model suggests a vertically coherent deformation across the entire lithosphere, while the second model implies little deformation in the upper crust since it explains crustal thickening and uplifting by inflation due to injection of middle and lower crustal material from the

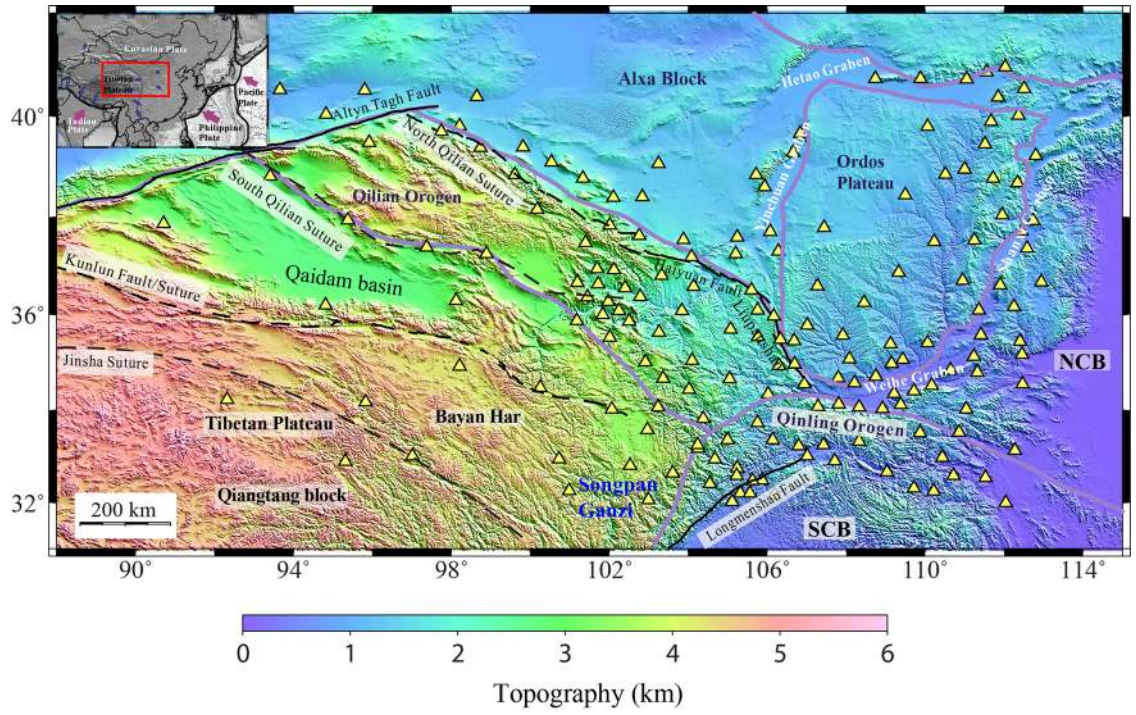

Figure 1. Geographic locations of the CEA stations (yellow triangles) are shown with topography of the NE Tibetan plateau and the surrounding area. The thick purple lines indicate the boundaries of different tectonic block, and the dashed black lines show the major sutures and faults within the NE Tibet. The inset in the top left corner shows the tectonic map of East Asia with the red box showing the location of our study area. The purple arrows represent the subduction of the Pacific and Philippine plates as well as the collision of the Indian plate at the east and southwest sides of China, respectively. The blue arrows indicate the GPS vectors (Gan *et al.* 2007). NCB and SCB stand for North China Block and South China Block, respectively.

center to the corner. Since the two models predict different seismic structures in the middle and lower crustal depths, various types of seismic data have been used to show which model is more suitable to explain the observed crustal thickening occurring beneath the eastern Tibet.

First, seismic tomography (e.g. Wang *et al.* 2003; Huang *et al.* 2010; Yao *et al.* 2010; Li *et al.* 2012; Yang *et al.* 2012; Liu *et al.* 2014; Wang & Gao 2014) has been used to identify a lower velocity layer associated with the hypothetic channel flow. The *P*- and *S*-wave tomography (Wang *et al.* 2003) showed significant low velocity anomalies in the middle and lower crustal level beneath the SE Tibet. The distribution of these slow anomalies, however, is not uniform as expected by the channel flow model, but is rather complicated. The similar feature is also shown in the surface wave tomography (e.g. Yao *et al.* 2010). On the other hand, Yang *et al.* (2012) obtained a large-scale low velocity anomaly at middle crust depths (∼15–30 km) beneath most of the plateau including eastern Tibet with ambient noise data. However such a continuous low velocity layer is not so obvious in other ambient noise tomography studies (Li *et al.* 2012; Liu *et al.* 2014).

Average crustal composition has been used as a proxy to differentiate the two models, since uniform lithospheric shortening preserves the original composition of a crustal column, while the lower crustal flow model predicts an overall mafic crust, as the thickened crust is comprised mainly of injected mafic lower crustal rocks. Pan & Niu (2011) measured *Vp*/*Vs* ratio across the NE margin of the Tibetan plateau and its surroundings with receiver function and found that the margin showed a systematically low *Vp*/*Vs* ratio. In general mafic rocks have higher *Vp*/*Vs* ratios than felsic rocks (Christensen 1996; Zandt & Ammon 1995). Thus they concluded that the crustal column beneath the margin is rather felsic, which is inconsistent with a scenario of an inflated crust due to extrusion of lower crust material from the central plateau to the margin.

Pervasive deformation can produce anisotropy on the scale of seismic wavelengths (e.g. Nicolas & Christensen 1987; Mainprice & Nicolas 1989). Measurements of seismic anisotropy thus can offer insight into the deformation kinematics within the Earth. Seismic anisotropy in earth's upper crust is generally believed to be caused by stress-induced alignment of cracks, which has been have been referred to as extensive-dilatancy anisotropy (EDA; Crampin & Peacock 2005). The cause of seismic anisotropy in the lower crust and mantle, on the other hand, is usually attributed to strain-induced lattice–preferred–orientation (LPO) of crustal and upper mantle minerals, such as mica, amphibole, and olivine (e.g. Zhang & Karato 1995; Meissner *et al.* 2002). Because of its close relationship with the stress–strain field, seismic anisotropy has been widely used to quantify subsurface deformation associated with a wide range of tectonic processes (Crampin & Lovell 1991; McNamara & Owens 1993; Silver 1996).

SKS waveform splitting has been measured across the NE Tibet to estimate seismic anisotropy. Li *et al.* (2011) and Wang *et al.* (2013) measured shear wave splitting of the core-refracted XKS waves recorded by tens of permanent broadband stations located in NE Tibet. They observed an average splitting time of ∼1.2 s with an NWW–SEE fast polarization direction, roughly parallel to the strike of the major thrust belts and perpendicular to the undergoing NNE–SSW horizontal shortening direction. Wang *et al.* (2013) interpreted the observed seismic anisotropy with lithospheric fabric associated with the present-day orogeny. Due to the low depth resolution of the core-refracted waves, it is difficult to determine which parts of the mantle the observed seismic anisotropy is distributed.

Generally, the Moho Ps converted phase, which can be extracted from receiver function analysis, is an ideal phase to study seismic anisotropy in the crust. Comparing to the XKS phase, this conversion wave is a much weaker signal, so finding a robust measurement of crust anisotropy is very important. Liu & Niu (2012) developed an integrated technique for estimating crustal anisotropy using radial and transverse receiver function data, which includes inversions with three individual and one joint objective function (JOF) and a reliability analysis of the estimated anisotropy. Sun *et al.* (2012) further added a harmonic analysis to the joint inversion method in order to enhance measurement robustness. They measured crustal anisotropy using receiver function data recorded at 79 broadband stations in the southeastern margin of the Tibetan plateau, and found significant seismic anisotropy at stations located inside the plateau. By comparing the seismic anisotropy estimated from SKS and receiver function data, Sun *et al.* (2012) concluded that the SE Tibet has been built by lower crustal flow and the mantle lithosphere beneath the margin may have been mechanically decoupled from the upper crust.

In this study, we focus on a complex junction that connects the margin of the Tibetan plateau with the Tarim basin, Alxa block, Ordos plateau and the Qinling orogenic belt, where broadband seismic data of 172 stations are available. We measure crustal anisotropy, Moho depth and crustal *Vp*/*Vs* ratio at these stations to investigate the lateral variations in crustal structure and deformation beneath the NE margin of the plateau and its surrounding areas. With the seismic data, we aim to better understand the plateau-forming processes occurring at the margin.

2 DATA AND ANALYSIS

2.1 CEA regional network data

To study lateral variations in crustal structure of the NE Tibetan plateau and its surrounding areas, we selected 172 stations from 9 CEA regional seismic networks (Gansu, Henan, Hubei, Inner Mongolia, Ningxia, Qinghai, Sichuan, Shanxi and Shaanxi) located within a rectangular region between 88° and 115° east, and 31° to 42° north (Fig. 1), which include 168 permanent stations and four temporary stations. We visually examined and selected a total of 797 teleseismic earthquakes with magnitude greater than 5.0 and an epicentral distance of 30–90°, recorded between August of 2007 and October of 2013. A large portion of the events are clustered in the western Pacific and the Java trench with a back azimuth between 30° and 210°, however, there is enough coverage of earthquakes in other directions (Fig. 2).

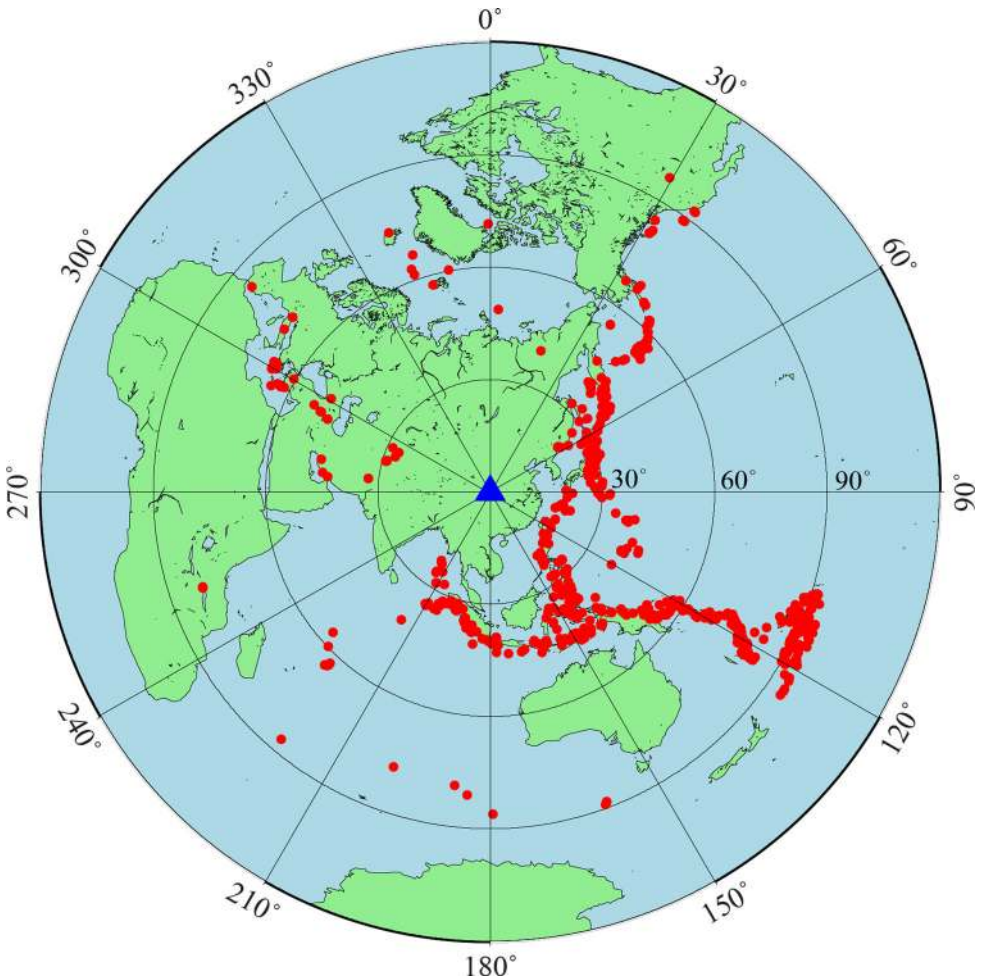

Figure 2. Locations of 797-teleseismicevents (red solid circles) used in this study. Most of the earthquakes are located in the western and southern Pacific, as well as the Indonesia subduction zones. Note that although some events fall into the 30° circle from the array center, all the seismograms we used have an epicentral distance between 30° and 90°.

2.2 Receiver functions

To generate receiver functions, we first rotated the two horizontal components of the 3-componenet seismograms into the radial (*R*) and transverse (*T*) components. Niu & Li (2011) found that a significant portion of the CEA regional network stations has orientation problems. Thus we used their method to compute sensor orientation for each station before conducting the rotation. We further projected the R and T components to the principal directions (longitudinal and in-plane transverse, hereafter to as P and SV components) (Vinnik 1977; Niu & Kawakatsu 1998), computed from the covariance matrix derived from the P arrival time window. The receiver functions were then computed based on both the *R–Z* (radial–vertical) and the *P–SV* combinations. We employed the 'water-level' deconvolution technique to generate R, T and SV receiver functions (Ammon 1991; Pan & Niu 2011). We then used the R and SV receiver functions for the *H–κ* analysis, and the R and T receiver functions for crustal anisotropy estimation. We visually inspected all the receiver functions and removed those with low SNR. At each station, we further calculated the covariance matrix of all the receiver functions and eliminated those that show a low cross correlation coefficient (<0.7) with other traces (Chen *et al.* 2010). The number of receiver functions selected at these stations varies from 24 to 564, with an average of ∼393. The total number of receiver functions used in the final analysis is 67 679.

As mentioned above, the main goal of this study is to determine azimuthal crustal anisotropy beneath the seismic stations. We applied the analyses developed by the Liu & Niu (2012) and Sun *et al.* (2012), which aim to make robust estimates of azimuthal seismic anisotropy, to the R–T receiver function data gathered at the 172 stations. The analyses include four major steps: (1) use *H–κ* stacking to obtain estimates of crustal thickness and *Vp*/*Vs* ratio; (2) make distance moveout correction to the Ps arrival time based on the estimated crustal thickness; (3) perform harmonic analysis to identify stations whose receiver functions exhibit significant azimuthal anisotropy; (4) estimate the polarization direction of the fast *S*-wave and delay time by a joint inversion of the R and T receiver functions. In the following four sections, we review the major analyses that they proposed to better constrain azimuthal anisotropy with receiver function data.

2.3 Depth stacking and *H–κ* analysis

Following Niu *et al.* (2007), we took two steps to determine the Moho depth and the average *Vp*/*Vs* ratio of the crust beneath each station. Firstly, we used a depth stacking method to determine an initial depth of the Moho beneath a station. Then we employed a refined *H–κ* analysis to determine the final depth and *Vp*/*Vs* that best explain the observed arrival time and amplitude of the Moho Ps conversion and the reverberation phases.

To obtain the initial depth, we first gathered receiver functions recorded at each station and made a time-to-depth conversion by assuming that *P* to *S* conversions are the primary sources of energy in the *P*-wave coda window. For a conversion depth, *d*, we first computed the relative arrival time of the converted phase, *Pds*, with respect to the direct arrival by ray tracing the two phases using a modified 1-D iasp91 velocity model (Kennett & Engdahl 1991), which has a crust extending to the depth *d*. We then stacked the receiver functions based on the calculated *Pds* moveouts using both linear and nonlinear stacking technique (Muirhead 1968; Kawakatsu & Niu 1994). We varied *d* from 0 to 100 km at an increment of 1 km and defined the depth with maximum stacking amplitude as the initial Moho depth.

Niu *et al.* (2007) introduced a coherence index of the three phases to make *H–κ* analysis, which include the primary *Ps* conversion phase, *0p1s* (Niu & James 2002), and the two crustal multiples, *2p1s* and *1p2s*, with respect to the direct *P* wave. The receiver functions were stacked using the following equation:

$$s(H,k) = \frac{c(x)}{N}\sum_{i=1}^{N}\{w_1 r_i(t_1) + w_2 r_i(t_2) + w_3 r_i(t_3)\}. \quad (1)$$

Here N is the number of receiver functions at a given station and $r_i(t)$ represents the amplitude of the ith receiver function at the calculated arrival times of the *0p1s*(t_1), *2p1s*(t_2) and *1p2s*(t_3). w_1, w_2 and w_3 are the weights of the three phases, which were assigned to 0.5, 0.25 and 0.25, respectively. Meanwhile, we also used all the combinations of the three phases in the *H–κ* stacking: (1) including all three phases, (2) using *0p1s* and *1p2s* phases, and (3) *0p1s* and *2p1s* phases to ensure measurement consistency. We searched for H within ±20 km of the initial depth determined from the depth stacking. κ was varied in the range of 1.5–2.0 with an increment of 0.001. H and κ were determined when the summed amplitude, $s(H, \kappa)$, reaches its maximum. For each station, we used a 1-D *P*-wave velocity model derived from a 3-D traveltime tomography study by Sun & Toksoz (2006). The *H–κ* estimated depths could differ from the initial values by a few kilometres depending on the difference between the measured and assumed *Vp*/*Vs* ratio.

The *H–κ* stacking result at GS.BYT is shown in Fig. 3(a), which exhibits a well-defined peak at $H = 52.3$ km and $\kappa = 1.674$. We further employed the τ–p analysis (Kawakatsu & Niu 1994) to confirm the correct identification of the Ps and multiples. Based on their ray paths, these two types of arrivals are expected to have a slightly lower and higher ray parameter (horizontal slowness) than the direct *P* wave, respectively. In order to determine the relative slowness of the *Ps* and multiples, we computed the vespagram of the two sets of receiver functions. We stacked the receiver functions with linear moveout corrections corresponding to a range of slownesses. The measured slowness of the Ps and multiples are indeed negative and positive (Fig. 3b), respectively.

2.4 Distance moveout correction

Since the Moho Ps conversion phase has a slightly smaller ray parameter than the direct *P* wave does, the relative arrival time of the Ps phase with respect to the *P* wave has a negative moveout. We used measured crustal thickness and *Vp*/*Vs* from the above *H–κ* stacking to compute the moveout for each station, and then made corrections so that all the Ps phases have a relative arrival time equivalent to the one with an epicentral distance of 60° and a source depth of 0 km. A more detailed description on how to make the correction can be found at Chen & Niu (2013). We further normalized the R and T receiver functions by dividing them with the peak amplitude of the *P* wave on the R component. After the moveout correction and the normalization, the R and T receiver functions are plotted as a function of back azimuth to detect systematic variations in the peak *Ps* arrival time and polarity changes in the R and T receiver functions.

2.5 Harmonic analysis of the Moho Ps arrival time

We applied the harmonic analysis proposed by Sun *et al.* (2012) to determine how the Moho *Ps* arrival time varies with back azimuth.

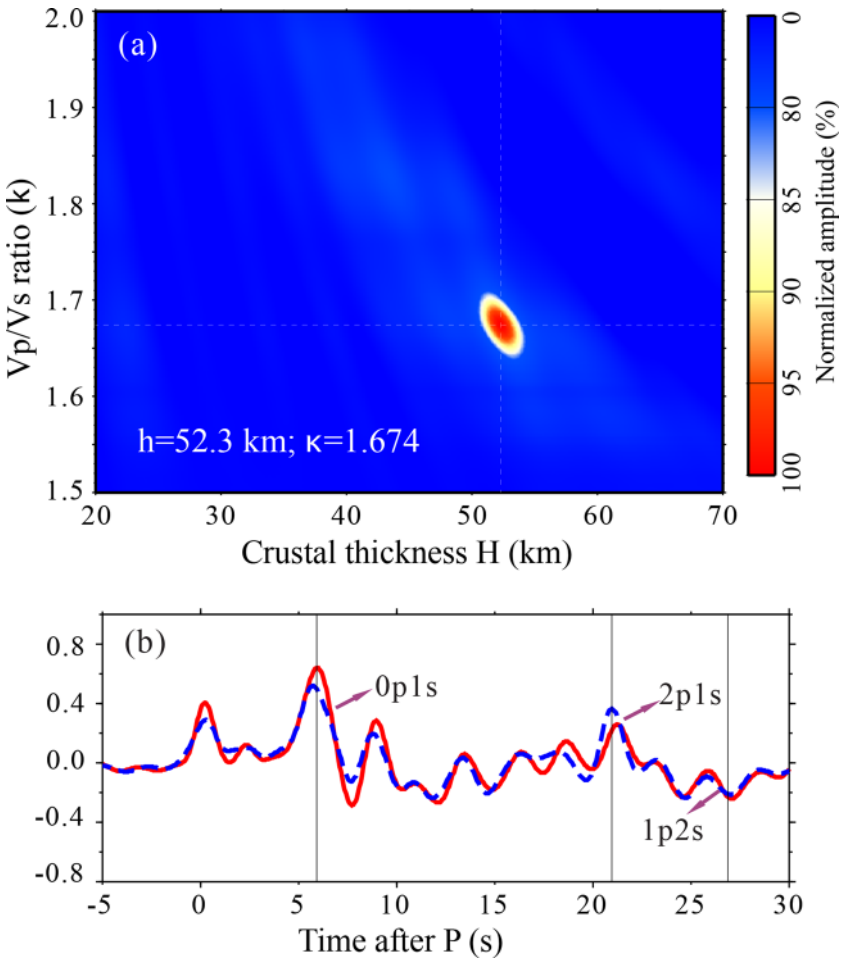

Figure 3. (a) An example of the *H*–κ analysis results at station GS.BYT. Color contours show the summed amplitude of the three phases as a function of crustal thickness and *Vp*/*Vs* ratio. Location of the amplitude peak is indicated by the two white lines. (b) Stacked receiver functions with the Ps slowness (red solid line) and the *2p1s* slowness (blue dashed line). Note that amplitude of the phases is larger when they are stacked with the correct slowness.

Assuming a harmonic degree, n, with peak-to-peak amplitude of δt, and initial phase of φ, we first computed the harmonic moveout correction at a station with a back azimuth of θ_i. We then stack all the R receiver functions after correcting the harmonic moveout. Finally, we computed normalized maximum amplitude, maximum energy of the stacked receiver function, and minimum total residual between each receiver function and the stacked receiver function. We varied n from 1 to 8, φ in the range of 0° to 360° with an increment of 1° and δt from 0.0 to 1.5 s in increments of 0.02 s. Fig. 4 shows the result of the harmonic analysis at GS.BYT. The maximum amplitude and energy of the stacked receiver function, as well the best fit between the stacked and individual receiver functions all showed a distinct peak at $n = 2$, suggesting the presence of azimuthal anisotropy inside the crust underneath the station.

Many studies (Levin & Park 1997; Peng & Humphreys 1997; Savage 1998; Shiomi & Park 2008) have shown that inhomogeneous crustal structures and various types of anisotropy can lead to different azimuthal variations in Moho Ps arrival time. For example, a dipping Moho or an anisotropic crustal layer with an inclined symmetry axis, can result in an $n = 1$ back azimuthal variation. If the anisotropic layer has a horizontal symmetry axis, then Ps time dependence on back azimuth is expected to be a four-lobed pattern, that is, $n = 2$. On the other hand, small-scale azimuthal variations in crustal velocity and Moho topography may result in higher order harmonic variations.

2.6 Estimate of crustal anisotropy

Most previous crustal anisotropy studies with receiver function data employed more or less the same techniques developed for SKS splitting analysis (McNamara & Owens 1993; McNamara *et al.* 1994; Iidaka & Niu 2001), which involves a grid search of the fast polarization direction (φ) and delay time (δt) between the fast and slow directions that either minimize the T component energy or maximize the cross correlation between the time-corrected fast and slow components. In this study, we used the method developed by Liu & Niu (2012), which includes jointly inverting R and T receiver function data with three individual and one joint objective functions, and a statistical analysis of the reliability on the estimated anisotropy.

The individual objective functions (IOFs) are designed to search for a pair of φ and δt that: (1) maximize the peak energy of the stacked R receiver function after a cosine moveout correction in the Ps arrival time; or (2) maximize the cross-correlation of the radial receiver functions after a full correction of crustal anisotropy or (3) minimize the total energy of transverse receiver functions stacked after removal of crustal anisotropy. The joint objective function (JOF) is computed by taking the average of the three IOFs, while the statistical analysis utilizes the principle that stacking a total of N coherent signals can lead to an increase of SNR by a factor of $N^{1/2}$, which can make full usage of the fingerprint of anisotropy on

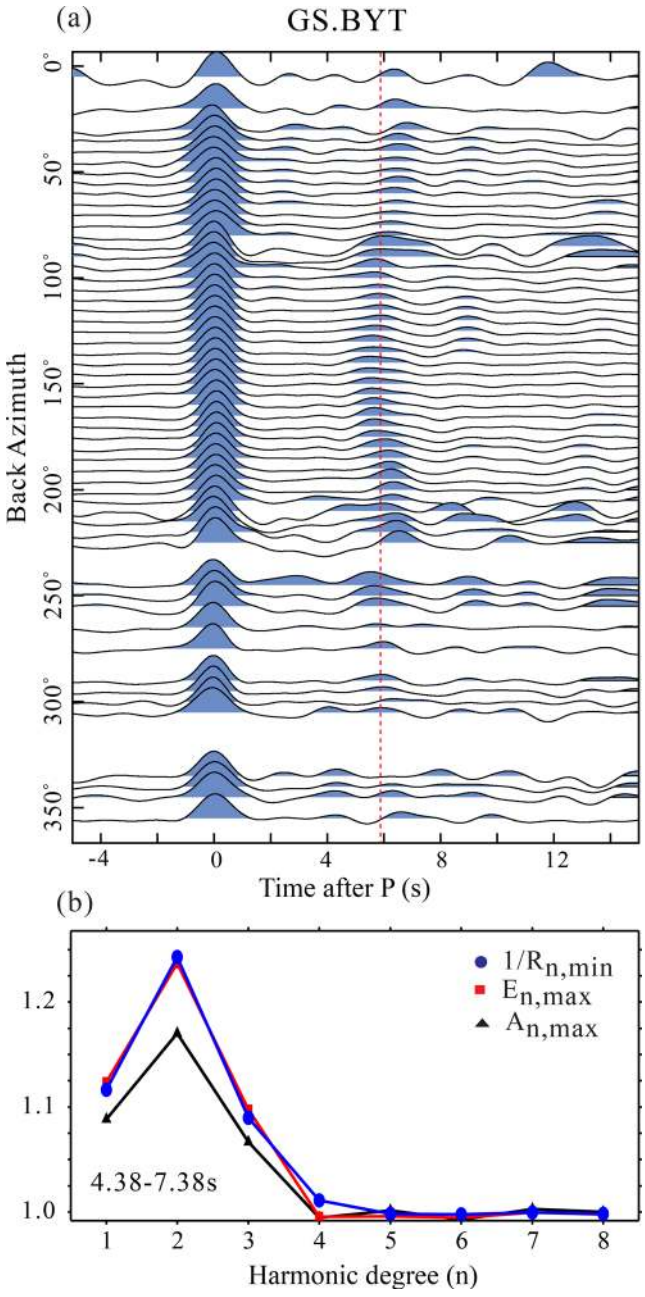

Figure 4. (a) R receiver functions recorded at station GS.BYT are plotted as a function of back azimuth. The receiver functions here are stacked in 10° bins along the back azimuth direction. Red dots indicate the arrival times of the Moho Ps conversion. (b) Results of the harmonic analysis at the same station. The maximum values of peak amplitude and total energy, as well as the reciprocal of the minimum residual are shown as a function of the harmonic degree.

receiver functions. More details on the method can be found in Liu & Niu (2012).

The three IOFs and the JOF computed at the station GS.BYT are shown in Fig. 5. The fast polarization direction and the splitting time estimated from the three methods are in agreement with each other, and the JOF estimate appears to be close to their average. Results of the statistical analysis on the measurement reliability based on the T and R receiver functions are shown in Figs 5(e) and (f), respectively. For the T receiver functions, the SNR of the data stacked after a correction of waveform polarity roughly increases linearly with $N^{1/2}$ (open squares in Fig. 5e) while the SNR of those stacked without a correction of waveform polarity remains nearly flat across the whole range of $N^{1/2}$ (open circles in Fig. 5e). On the other hand, if anisotropy is removed, the T receiver functions are composed primarily of random noise. Therefore, no matter whether a polarity correction (filled squared in Fig. 5e) is applied or not (open circle in Fig. 5e), the SNR does not change with $N^{1/2}$. Meanwhile, when significant anisotropy is present, the stacked R receiver functions after the correction of crustal anisotropy (filled triangles in Fig. 5f) are expected to have a larger SNR than those without correction (open triangles in Fig. 5f).

3 RESULTS

3.1 Crustal thickness and *Vp*/*Vs* ratio

Among the 172 stations, we were able to obtain 171 measurements of crustal thickness and *Vp*/*Vs* ratio (Supporting Information Figs S1 and S2). The estimated (H, κ) are listed in Supporting Information Table S1. The table is organized by grouping stations in the following tectonic regions: the Tibetan plateau (TP), the Qilian orogenic belt (QL) and the Qinling orogenic belt (QB), the Ordos plateau (OP), the Weihe graben (WG) and the North China plain (NP).

We further employed the inversion method proposed by Niu *et al.* (2007) to interpolate the 171 measurements and generate 2-D relief maps for the Moho depth and *Vp*/*Vs* ratio, respectively. We divided the study area from 32° to 41°N (latitude) and 90° E to 113°E (longitude) into meshed grids of 0.25° × 0.25°. There are 37 and 93 gridpoints in the latitude and longitude directions within the study area. This gives a total of 3441 unknown parameters of Moho depth inverted from 171 observations. A regularization that minimizes the first derivative of the model was added to regularize the underdetermined inversion. The results are shown in Fig. 6. Since station spacing varies from 9 to 315 km with an average of 66 km, thus the actual resolution is probably not as high as the 0.25° × 0.25° grid spacing. Moreover, the maps have no resolution in the corner regions due to lack of station coverage, thus, they may not reflect the true values of the Moho depth and *Vp*/*Vs* ratio in these regions.

The eastern part of our study area overlaps with that of Pan & Niu (2011), and we found that a large portion of the 171 stations (113 stations) were analysed by them. In general, our measurements are in good agreement with their results except for five stations. Since they only used one-year data, we think that the small number of receiver functions used in their study may have caused this discrepancy. Most of the new stations are located on the Qilian orogenic belt with only a few being located on the inner part of the plateau (Bayan Har and Qiangtang blocks) and not a single station inside the Qaidam basin. Zhu & Helmberger (1998) investigated waveform data in the area and found a 15–20 km Moho offset across the eastern Kunlun fault, suggesting that the Qaidam basin has a 15-20 km shallower Moho than the plateau does. Therefore, we consider the deep Moho and relatively low *Vp*/*Vs* ratio beneath the Qaidam basin shown in Fig. 6 to be related to interpolation biases. This is probably also true for the Qinghai Lake.

In general, the resulting Moho depth shows significant variations across the study area, varying from 31.3 to 71.3 km an average depth of 45.9 km (Fig. 6a). The shallowest Moho is observed at SN.LINT at the Weihe graben in the southern edge of the Ordos plateau, while the thickest crust is located beneath the stations QH.QML in the central part of Tibetan plateau. Meanwhile, the Moho also appears to follow the changes in surface topography, and shows

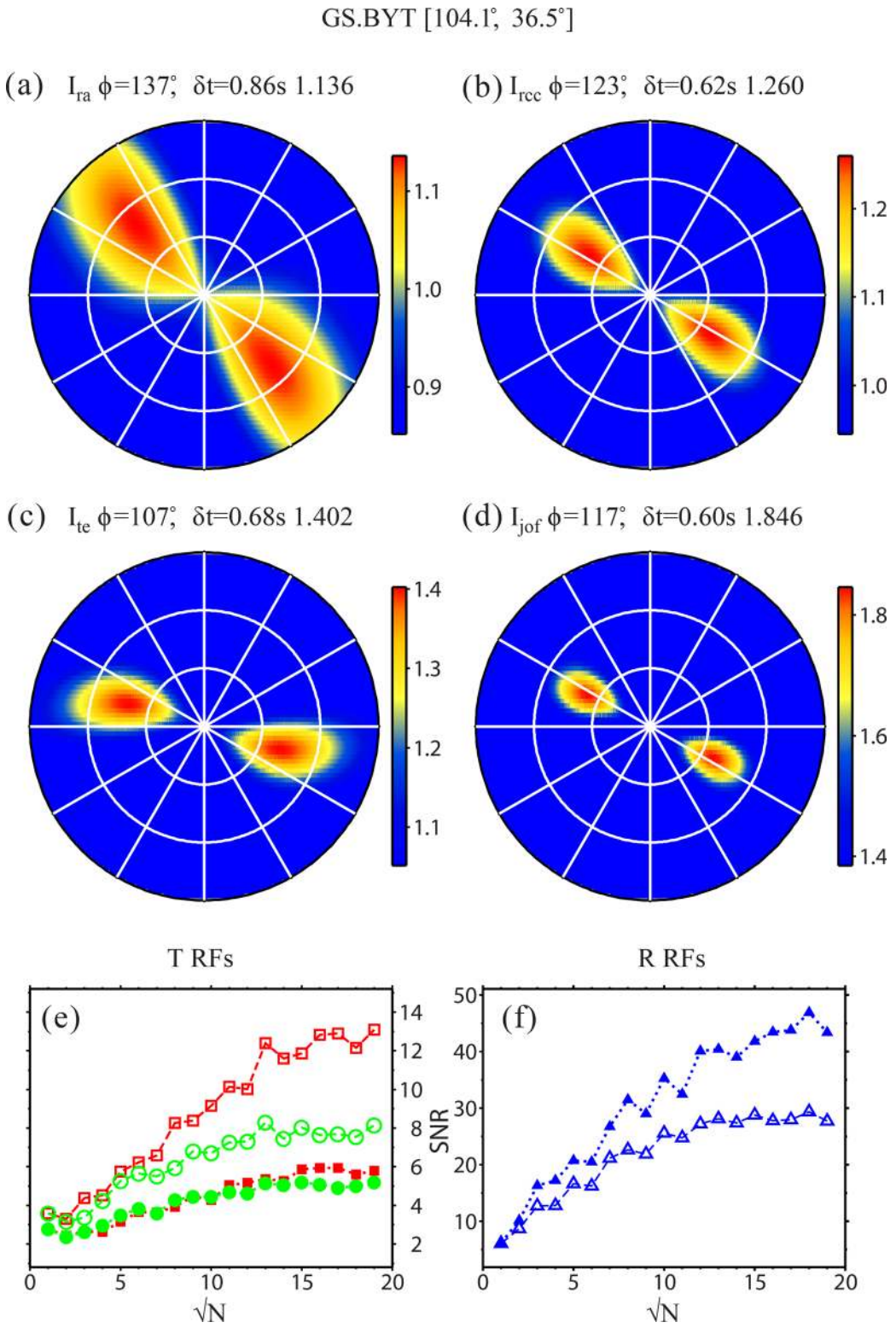

Figure 5. Results from the joint analysis of crustal anisotropy with multicomponent receiver function data at station GS.BYT. (a), (b) and (c) correspond to three different methods for estimating seismic anisotropy: (1) R energy maximization with a cosine moveout correction; (2) radial cc maximization and (c) T energy minimization (represented by maximizing the inverse of T energy). Color scales showing variations of the objective functions are plotted to the right of the functions. The JOF is shown in (d). The objective functions were computed in a 2-D plane of (φ, δt) in the range of (0°–360°, 0.0–1.5s) with an increment of (1°, 0.02s). Panels (e) and (f) show the reliability analysis of the estimated anisotropy with the T and R receiver function data, respectively. Open and filled symbols in (e) and (f) represent SNR calculated from stacks of receiver functions before and after the removal of seismic anisotropy determined by the JOF. Note the steady increase of square (stack with a sign correction of backazimuth) with increasing $N^{1/2}$ in (e) and that the filled triangles are always above the open ones in (f).

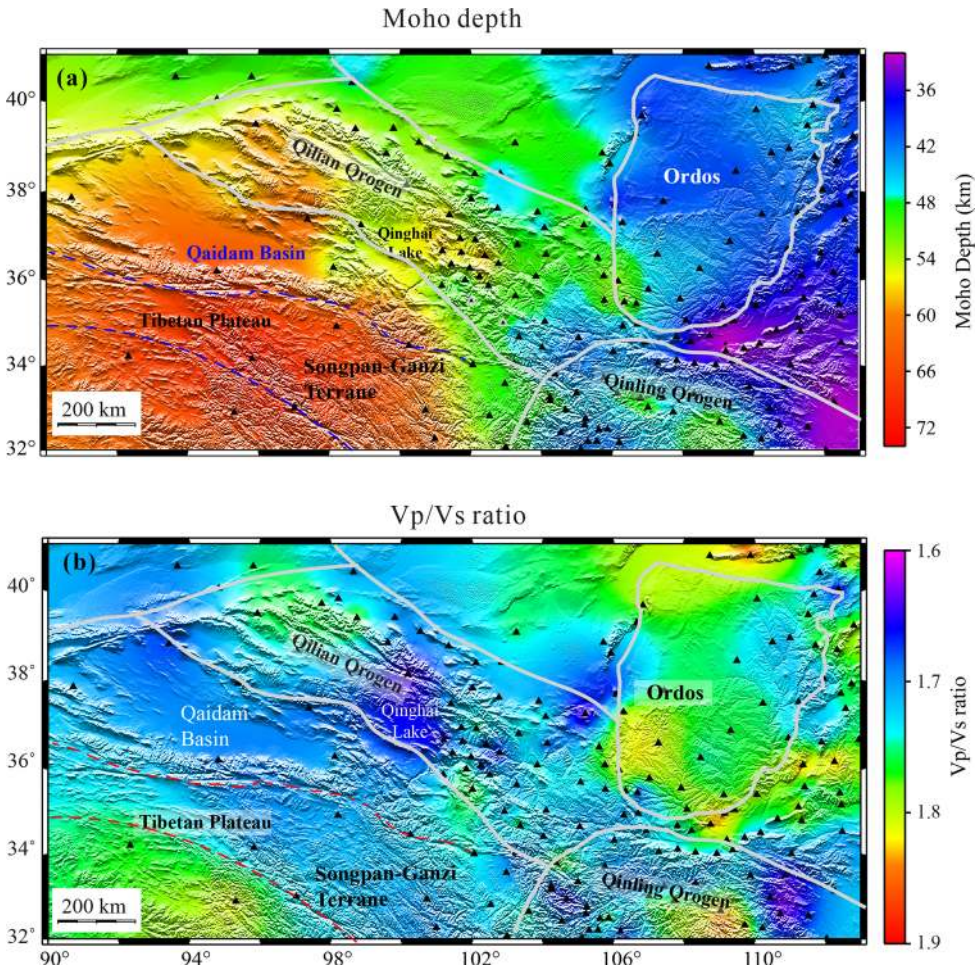

Figure 6. Panels (a) and (b) show the Moho relief and *Vp*/*Vs* ratio map inverted from observations at stations shown as black triangles. Note the gradual increase of Moho depth from east to west in (a) and the remarkable contrast between the NE Tibet (Bayan Har block and Qilian orogen) and its neighbors: the Ordos plateau to the northeast and the central Tibet (Qiangtang block) to the south in (b).

gradually deepening from east to west. Overall there is a positive correlation between Moho depth and station elevation, and a simple linear regression of the two shows a coefficient of determination of $R^2 = 0.67$. The linear relationship appears to still hold in the present-day orogenies, such as the Qiangtang and Bayan Har blocks of the Tibetan plateau, and the Qilian orogen, but not in the past orogenies, such as the Proterozoic Qinling orogenic belt and the Ordos plateau.

The *Vp*/*Vs* ratio map showed in Fig. 6(b) shows remarkable differences among different tectonic regions. The Qiangtang block in the heartland of the Tibetan plateau and the Ordos plateau have an average *Vp*/*Vs* ratio of 1.752 and 1.794 with a standard deviation of 0.037 and 0.024, respectively, while the Bayan Har block of the Tibetan plateau, the Qilian and Qinling thrust belts exhibit a *Vp*/*Vs* ratio as low as 1.707 ± 0.023, 1.719 ± 0.035 and 1.718 ± 0.035, respectively. As mentioned above, although the Qaidam basin shows low *Vp*/*Vs* ratio in Fig. 6(b), this is likely caused by interpolation.

3.2 Crustal anisotropy

The estimates of harmonic degree, apparent fast direction and splitting time, as well as the SNR statistical analysis results are also shown in Table S1. Among the 171 stations with (H, κ) measurements, nine stations do not have enough back azimuthal coverage for anisotropy analysis, which are indicated with 'X' in the last three columns. Three stations (QH.ZAD, QH.QIL and GS.ZYT) have an apparent splitting time greater than the maximum time shift (1.5 s), which is considered to be unreliable and listed with (999, 9.99) in Table S1. In the harmonic degree column, we use '0' to indicate those stations with a broad distribution in the harmonic degree space. A total of 35 stations exhibit this pattern, suggesting that multiple structures, such as a dipping Moho, small-scale heterogeneities, and seismic anisotropy likely coexist in the crust beneath these stations.

For the rest 124 stations, 47 and 26 stations have a harmonic order of $n = 1$ and $n = 2$, respectively; 16 stations have a harmonic order greater than 2 and 34 stations exhibit a bimodal distribution, centering mainly on degree 1 and degree 2. Most of the stations with a degree-1 back azimuthal variation in the Moho Ps arrival time are located inside the Qilian and Qinling orogenic belts where the crust is highly deformed. As mentioned above, a dipping Moho or an anisotropic crustal layer with an inclined symmetry axis, can result in an $n = 1$ back azimuthal variation. This strong degree-1 variation can mask the degree-2 anisotropic signal, and therefore affect the extraction of azimuthal anisotropy from the receiver function data. Future studies on how to obtain robust seismic anisotropy from this type of stations are required.

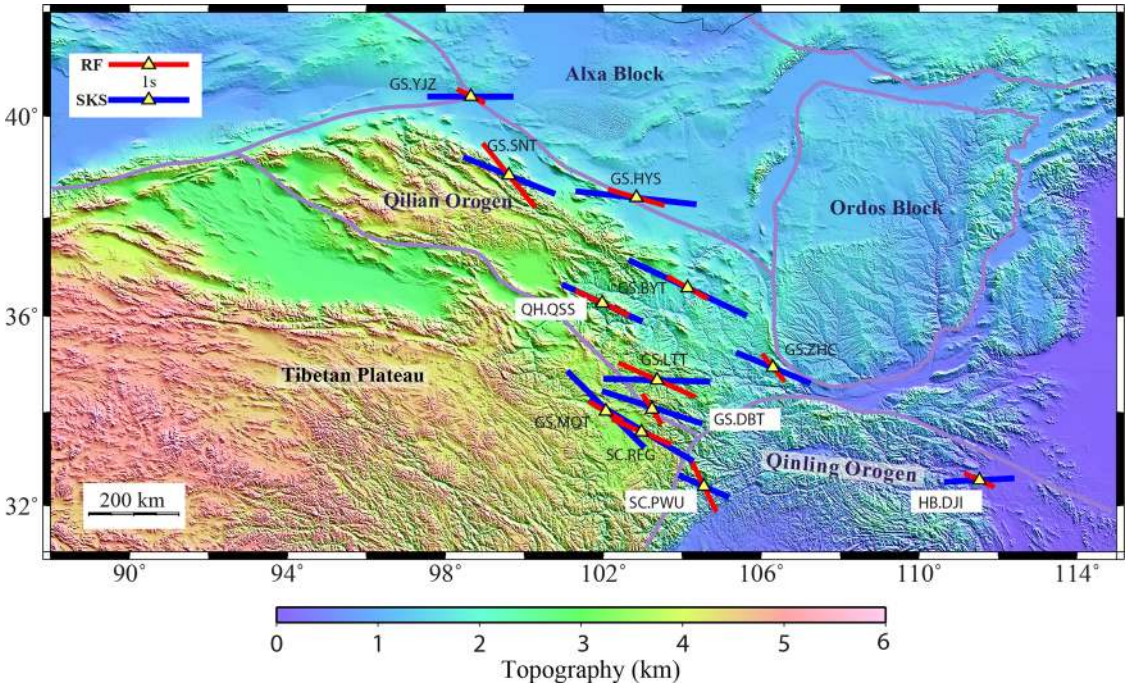

Figure 7. Map showing the splitting measurements at 12 stations based on Moho Ps (red bars) and SKS/SKKS data (blue bars). The SKS/SKKS measurements are taken from Wang *et al.* (2013). The fast orientation bars are centered at the stations and their length indicates the amount of splitting.

We found that the crustal structure beneath 12 stations shows a robust and significant azimuthal anisotropic component. We define a robust measurement when the Moho Ps arrival time possesses a degree-2 backazimuthal variation, and there is a significant difference between receiver functions before and after anisotropic corrections. For stations located above an isotropic or a weakly anisotropic crust, the Moho Ps arrivals would not show these two features; therefore, no robust measurements are anticipated at these stations. We found that 44 stations have an apparent splitting time less than 0.2 s. These stations are mainly located inside the less deformed Ordos plateau, the north China plateau and the Alxa block (Fig. 1).

The measured fast polarization direction and the splitting time at the 12 stations are shown in Fig. 7 and are also highlighted in Table S1. In general, all the 12 stations tend to have an NWW–SEE or NW–SE fast polarization direction, which is in good agreement with the strike direction of the faults and orogenies in the area. The splitting time between the fast and slow waves varies from 0.36 to 1.06s with an average of 0.64s. Among the 12 stations, 5 stations (GS.YJZ, GS.SNT, GS.HYS, GS.BYT and QH.QSS) are located in and around the Qilian orogen, and another five stations (GS.LTT, GS.DBT, GS.MQT, SC.REG and SC.PWU) are in the transition zone beneath the Tibetan and Ordos plateaus. The other two lie in the southern margin of the Ordos (GS.ZHC) and the eastern part of the Qinling orogen (HB.DJI), respectively. We noticed that the observed fast polarization direction here roughly aligns with the orientation of the maximum horizontal tensile stress of the area (Flesch *et al.* 2001).

4 DISCUSSION

4.1 Constraints on deformation mechanism

Pan & Niu (2011) noticed the low crustal *Vp*/*Vs* ratio beneath the NE corner of Tibetan plateau and used it to argue against the middle and lower crustal channel flow model as the cause of the crustal thickening in NE Tibet. We found that this feature of low crustal *Vp*/*Vs* ratio seems to be true across the entire NE margin including the Bayan Har tectonic block and the Qilian orogen (and probably except for the Qaidam basin where we have no data coverage). Further south, the Qiangtang block shows a remarkable difference from its northern neighbors with a very high *Vp*/*Vs* ratio of 1.794. It has been shown that a ∼5 per cent error in the assumed *Vp* has almost negligible effect on the estimated *Vp*/*Vs* ratio (e.g. Zhu & Kanamori 2000; Nair *et al.* 2006; Chen *et al.* 2010), thus the observed *Vp*/*Vs* ratio contrast here is unlikely caused by the reference velocity model.

Laboratory studies indicated that the compressional and shear wave velocity ratio, *Vp*/*Vs*, is a good indicator of crustal composition (e.g. Christensen 1996). Under pressure and temperature conditions that are far below the solidus, the two appear to have insignificant effect on the *Vp*/*Vs* ratio. The relative abundance of quartz (*Vp*/*Vs* = 1.49) and plagioclase (*Vp*/*Vs* = 1.87) appears to a dominant effect on the *Vp*/*Vs* ratio of common igneous rocks and their metamorphosed equivalents. An increase in plagioclase content or a decrease in quartz content can increase the *Vp*/*Vs* ratio of a rock. For example, the *Vp*/*Vs* ratio increases from 1.710 for granitic rock, to 1.780 for diorite and to 1.870 for gabbro (Tarkov & Vavakin 1982). The mafic/ultramafic igneous rocks generally have high *Vp*/*Vs* ratios because they usually contain gabbro and peridotite or dunite, which originate from magmatic differentiation. In addition to composition, partial melt seems to have an important effect on the *Vp*/*Vs* ratio, which significantly increases with an increasing fluid fraction (Watanabe 1993).

Pan & Niu (2011) argued that the observed low *Vp*/*Vs* beneath the NE Tibet is likely an indicative of felsic to intermediate composition of the crust beneath the two regions. Meanwhile, the lower crustal channel flow model predicts a crustal column in NE Tibet is primarily composed of lower crustal material from central plateau, and therefore the average crustal composition would be mafic, resulting in a high *Vp*/*Vs* ratio which is contradictory to the observation. Pan

& Niu (2011) further speculated that vertical coherent shortening might be the dominant mechanism responsible for the large surface uplifting and Moho deepening in NE Tibet. Here we found that the low *Vp*/*Vs* ratio area extends to the entire Qilian orogen and most of the Bayan Har tectonic block, which are consistent with their argument against the lower crust channel flow model. In addition, we consider our observation on crustal seismic anisotropy also argues favorably for the whole lithospheric shortening mechanism.

It should be noted that the 12 stations are very strictly selected from the 171 stations based on the two idealized criteria and this number should be considered as the most conservative estimates of stations with significant crustal anisotropy. For example, there are a total of 17 stations located inside the Tibet plateau, and only three measurements are counted as robust estimates. However, the estimated fast polarization direction and delay time at another nine stations are roughly similar to the 3 measurements. We also checked internal consistence in the measured seismic anisotropy among neighboring stations. We found six are located within 50 km from the 12 stations, among which half showed compatible measurements with the 12 stations. The other three stations are characterized by a strong degree-1 back azimuthal variation, which might have affected the estimated fast direction and splitting time. We obtained roughly the similar statistics if we expanded the distance range to 80 km. Among the total of 32 stations located inside the 80-km range, 17 stations exhibit comparable fast directions and splitting times, while all the other 15 stations with different fast directions possess an $n = 1$ backazimuthal variation in the harmonic analysis. Therefore it is likely that the 12 measurements reflect the regional anisotropy of the NE margin.

The *S*-wave ray path of the Moho Ps conversion goes from the Moho to the surface, thus the estimated anisotropy can in principle be anywhere along the path. As the fast direction is almost perpendicular to the direction of the maximum horizontal compressional stress, we argue that it is unlikely caused by stress-induced alignment of cracks in the upper crust above ∼15 km, and is more likely the results of fabric structure developed in the middle and lower crust below ∼15 km. In fact, Zhang *et al.* (2012) measured the azimuthal anisotropy in the upper crust of the Qilian orogen using shallow local earthquakes with the SAM technique (Gao *et al.* 2008). They obtained a delay time of only ∼0.10–0.12s, which is significantly smaller than the estimates of ∼0.36–1.06s here. Thus the primary source for the observed anisotropy should lie in the middle and lower crust.

As mentioned above, seismic anisotropy in the deep crust is generally attributed to the LPO of anisotropic minerals in the lower crust, that is, amphibole. Experimental studies on the LPO of amphibole are limited. A recent study by Ko & Jung (2015) found that when amphibole is deformed by simple shear it produces three types of LPO structures, which possess strong seismic anisotropy. Type-II and Type-III produce fast polarization directions that are subparallel to the simple shear direction, which is close to the type of LPO structure observed for olivine under simple shear conditions. Since there is no experimental data on pure shear deformation of amphibolite at high pressure and temperature conditions, it is still difficult to assert that the collision induced SW–NE compression is the likely cause of the observed seismic anisotropy here. However, we view the collision related pure shear as a viable mechanism for the observed mechanism if we assume amphibole deforms similarly to olivine by pure shear.

Wang *et al.* (2013) also measured the shear wave splitting with XKS data recorded at the 12 stations, and obtained an average splitting time of 1.22 s, which is approximately twice as large as what we observed here. A station-by-station comparison of the fast polarization direction and splitting time estimated from the Moho Ps and the XKS phases are shown in Fig. 7. In general, most of the stations show similar fast polarization directions derived from the two phases, and the XKS splitting times are slightly larger than those of the Moho Ps phase. Li *et al.* (2011) measured shear wave splitting with XKS recorded at a large number stations in the area and found that most of the splitting can be explained by a one layered anisotropic model. The agreement in the measured fast polarization direction between the receiver function and the XKS data is consistent with their interpretation. It further suggests that crustal anisotropy plays an important role in explaining the observed XKS splitting, which is likely caused by vertically coherent deformation within the lithosphere.

In summary, the crust beneath the NE Tibetan shows the following two distinct seismic features: (1) it has a significantly lower *Vp*/*Vs* ratio compared with its surroundings, such as the Ordos plateau and central Tibet; (2) it has a strong azimuthal anisotropy, with a fast direction roughly parallel to the direction of the maximum horizontal tensile stress. These observations suggest that the thicken crust beneath NE Tibet is likely composed of felsic to intermediate rocks and lithospheric deformation is primarily driven by vertically coherent shortening associated with the India-Asia collision (Fig. 8).

4.2 A comparison with SE Tibet

Clark & Royden (2000) suggested that the large-scale morphology of the eastern plateau can be largely modeled by an eastward fluid flow within the middle to lower crust that is driven by the elevation contrast between the plateau and its surroundings. This eastward flow runs into the strong crust of the Sichuan basin at its front and diverges into two branches (Fig. 8a). The southern branch flows around the southwest side of the Sichuan basin, and finally into the SE margin of the Tibetan plateau, while the northern branch appears to be further guided by the strong crust of the Qaidam basin in the west and flows toward northeast into the Ordos plateau (Fig. 8a).

While this scenario seems to be inconsistent with the crustal velocity and anisotropic structure observed in NE Tibetan, there is compelling evidence that this is occurring within the crust beneath SE Tibet. Sun *et al.* (2012) found that the thick crust has a relatively higher *Vp*/*Vs* ratio compared to the global average (Christensen & Mooney 1995) beneath the SE Tibet, which was used to argue a mafic composition for the crust beneath the margin. They also found that the crust under the SE Tibet has large azimuthal anisotropy, indicating that the whole crust is highly deformed. Since the fast polarization direction of the *S* wave aligns roughly with the hypothetic lower crust flow direction proposed by Clark & Royden (2000), they interpreted the azimuthal anisotropy to be caused by the flow-induced lattice preferred orientation (LPO) of middle and lower crustal minerals, such as mica and amphibole (Fig. 8c).

5 CONCLUSION

We analysed a large amount of receiver function data to investigate crustal structure and seismic anisotropy beneath the NE Tibetan plateau and its surrounding areas. We found that the thick crust beneath the NE Tibetan plateau has a relatively low *Vp*/*Vs* ratio, suggesting that the crust is made of felsic to intermediate rocks. We also found that the middle and lower crust underneath the margin shows strong azimuthal seismic anisotropy, with

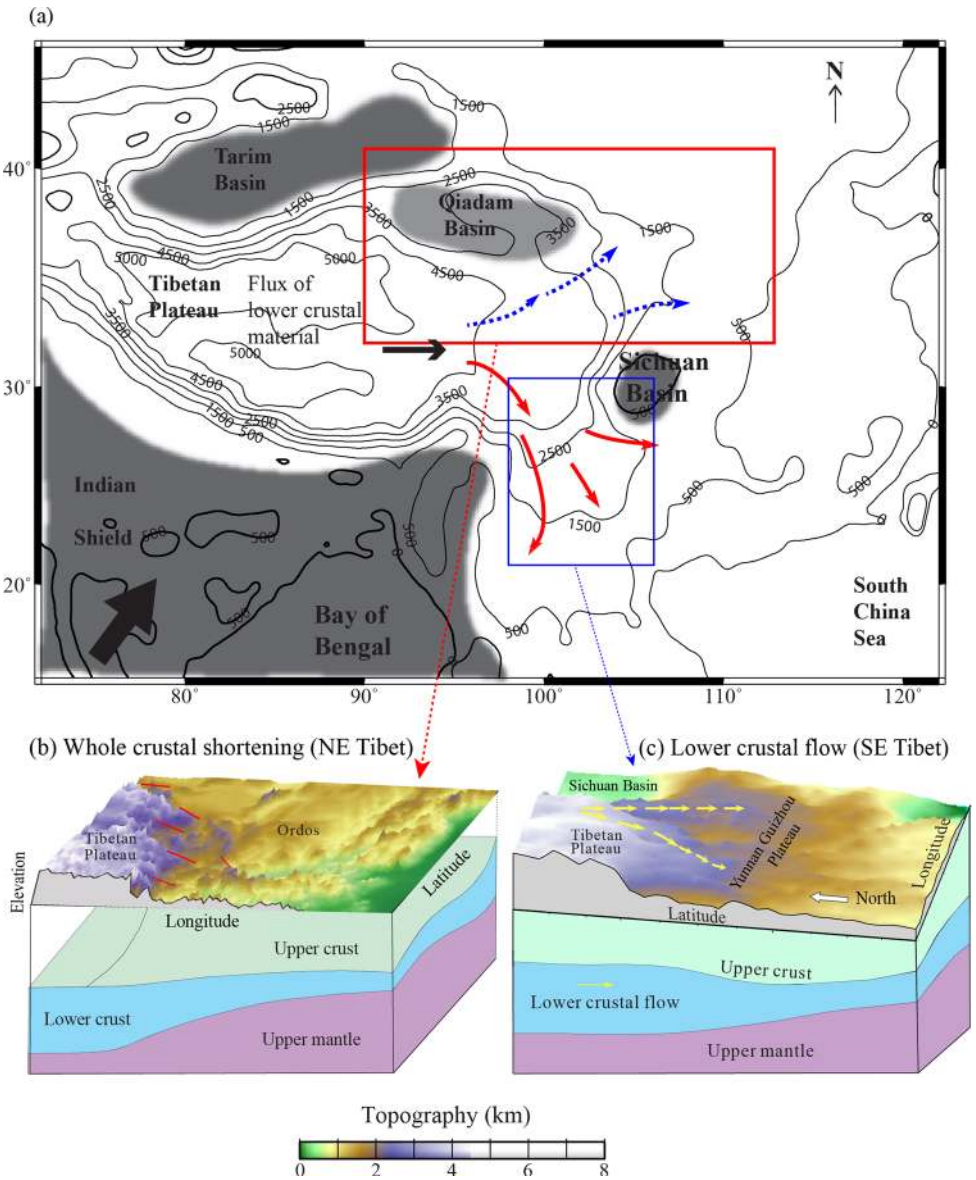

Figure 8. (a) Modified from Clark & Royden (2000). Contour plots of smoothed elevations of the Tibetan plateau and its surrounding areas. Arrows indicate the lower crustal flow proposed by Clark & Royden (2000). Blue and red boxes indicate the study area of Sun *et al.* (2012) (SE Tibet) and our study area (NE Tibet), respectively. Cartoons illustrate the two models: (b) whole crustal shortening model and (c) lower crustal flow model, for crustal thickening observed at the NE and SE Tibet, respectively.

the fast polarization directions roughly similar to those derived from XKS data. These observations suggest that the crust and mantle lithosphere are mechanically coupled and deformed coherently in responding to the India-Asia collision, and therefore the whole lithospheric shortening is likely the dominant mechanism for the observed large uplifting and crustal thickening within the margin.

ACKNOWLEDGEMENTS

We thank the Data Management Center of the China Earthquake Administration for providing the waveform data for this study. We also thank Min Chen, Steve Grand and Alan Levander for discussion. We also thank Dr Stephen Gao and another anonymous reviewer for their constructive comments and suggestions, which significantly improved the quality of this paper. QW and FN is supported by the NSFC project 41274099 and NSF grant 1345096, QW and YG is supported by the NSFC project 41474032 and China National Special Fund for Earthquake Scientific Research in Public Interest (201308011).

REFERENCES

Ammon, C.J., 1991. The isolation of receiver effects from teleseismic *P* waveforms, *Bull. seism. Soc. Am.,* **81**(6), 2504–2510.

Chen, Y. & Niu, F., 2013. Ray parameter based stacking and enhanced preconditioning for stable inversion of receiver function data, *Geophys. J. Int.,* **194,** 1682–1700, 2013.

Chen, Y., Niu, F., Liu, R.F., Huang, Z.B., Tkalcic, H., Sun, L. & Chan, W., 2010. Crustal structure beneath China from receiver function analysis. *J. geophys. Res.,* **115,** B03307, doi:10.1029/2009JB006386.

Christensen, N.I., 1996. Poisson's ratio and crustal seismology, *J. geophys.Res.,* **102,** 3139–3156.

Christensen, N.I. & Mooney, W.D., 1995. Seismic velocity structure and composition of the continental crust: a global view, *J. geophys. Res.,* **100,** 9761–9788.

Clark, M.K. & Royden, L.H., 2000. Topographic ooze: Building the eastern margin of Tibet by lower crustal flow, *Geolog,* **28,** 703–706.

Crampin, S. & Lovell, J., 1991. A decade of shear-wave splitting in the Earth's crust: what does it mean? What use can we make of it and what should we do next?, *Geophys. J. Int.,* **107**(3), 387–407.

Crampin, S. & Peacock, S., 2005. A review of shear-wave splitting in the compliant crack-critical anisotropicEarth, *Wave Motion,* **41,** 59–77.

Dewey, J.F., Shackleton, R.M., Chang, C.F. & Sun, Y.Y., 1988. The tectonic evolution of the Tibetan Plateau, *Phil. Trans. R. Soc. Lond.* A, **327**(1594), 379–413.

England, P. & Houseman, G., 1986. Finite strain calculations of continental deformation 2. Comparison with the India-Asia collision zone, *J. geophys. Res.,* **91**(B3), 3664–3676.

Flesch, L.M., Haines, A.J. & Holt, W.E., 2001. Dynamics of the India-Eurasia collision zone, *J. geophys. Res.,* **106,** 16 435–16 460.

Gan, W.J., Zhang, P.Z., Shen, Z.K., Niu, Z.H., Wang, M., Wan, Y.G., Zhou, D.M. & Cheng, J., 2007, Present-day crustal motion within the Tibetan plateau inferred from GPS measurements, *J. geophys. Res.,* **112**(B08416), doi: 10.1029/2005JB004120.

Gao, Y., Shi, Y.T., Liang, W., Liu, X.Q. & Hao, P., 2008. Systematic analysis method of Shear-wave splitting SAM (2007): software system, *Earthq. Res. China,* **24**(4), 345–353.

Huang, H., Yao, H. & van der Hilst, R.D., 2010. Radial anisotropy in the crust of SE Tibet and SW China from ambient noise interferometry, *Geophys. Res. Lett.,* **37,** L21310, doi:10.1029/2010GL044981.

Iidaka, T. & Niu, F., 2001. Mantle and crust anisotropy in the eastern China region inferred from waveform splitting of SKS and PpSms, *Earth Planets Space,* **53,** 159–168.

Kawakatsu, H. & Niu, F., 1994. Seismic evidence for a 920-km discontinuity in the mantle, *Nature,* **371,** 301–305.

Kennett, B. & Engdahl, E.R., 1991. Traveltimes for global earthquake location and phase identification, *Geophys. J. Int.,* **105,** 429–465.

Ko, B. & Jung, H., 2015. Crystal preferred orientation of an amphibole experimentally deformed by simple shear, *Nat. Commun.,* **6,** 6586, doi:10.1038/ncomms7586.

Levin, V. & Park, J., 1997. P-SH conversions in a flat-layered medium with anisotropy of arbitrary orientation, *Geophys. J. Int.,* **131,** 253–266.

Li, H.Y., Li, S., Song, X.D., Gong, M., Li, X. & Jia, J., 2012. Crustal and uppermost mantle velocity structure beneath northwestern China from seismic ambient noise tomography, *Geophys. J. Int.,* **188,** 131–143.

Li, Y., Wu, Q., Zhang, F., Feng, Q. & Zhang, R., 2011. Seismic anisotropy of the Northeastern Tibetan plateau from shear wave splitting analysis, *Earth planet. Sci. Lett.,* **304,** 147–157.

Liu, H. & Niu, F., 2012. Estimating crustal seismic anisotropy with a joint analysis of radial and transverse receiver function data, *Geophys. J. Int.,* **188,** 144–164.

Liu, Q.Y. *et al.* 2014. Eastward expansion of the Tibetan plateau by crustal flow and strain partitioning across faults, *Nat. Geosci.,***7,** 361–365.

Mainprice, D. & Nicolas, A., 1989. Development of shape and lattice preferred orientations: application to the seismic anisotropy of the lower crust, *J. Struct. Geol.,* **11,** 175–189.

McNamara, D. & Owens, T., 1993. Azimuthal shear wave velocity anisotropy in the basin and range Province using Moho Ps converted phases. *J. geophys. Res.,* **98,** 12003–12017.

McNamara, D.E., Owens, T.J., Silver, P.G. & Wu, F.T., 1994. Shear wave anisotropy beneath the Tibetan plateau, *J. geophys. Res.,* **99,** 13 655–13 665.

Meissner, R., Mooney, W.D. & Artemieva, I., 2002. Seismic anisotropy and mantle creep in young orogens, *Geophys. J. Int.,* **149,** 1–14.

Molnar, P. & Tapponnier, P., 1975. Cenozoic tectonics of Asia: effects of a continental collision, *Science,* **189,** 419–426.

Muirhead, K.J., 1968. Eliminating false alarms when detecting seismic eventsautomatically, *Nature,* **217,** 533–534.

Nair, S.K., Gao, S.S., Liu, K.H. & Silver, P.G., 2006, Southern African crustal evolution and composition: constraints from receiver function studies, *J. geophys. Res.,* **111,** B02304, doi:10.1029/2005JB003802.

Nicolas, A. & Christensen, N.I., 1987. Formation of anisotropy in upper mantle peridotites-a review, *Rev. Geophys.,* **25,** 111–123.

Niu, F. & James, D.E., 2002. Fine structure of the lower most crust beneath the Kaapvaal craton and its implications for crustal formation and evolution, *Earth planet. Sci. Lett.,* **200,** 121–130.

Niu, F. & Kawakatsu, H., 1998. Determination of the absolute depths of the mantle transition zone discontinuities beneath China: effect of stagnant slabs on transition zone discontinuities, *Earth Planets Space,* **50,** 965–976.

Niu, F. & Li, J., 2011. Component azimuths of the CEArray stations estimated from *P*-wave particle motion, *Earthq. Sci.,* **24,** 3–13.

Niu, F., Bravo, T., Gary, P., Vernon, F., Rendon, H., Bezada, M. & Levander, A., 2007. Receiver function study of the crustal structure of the southeastern Caribbean plate boundary and Venezuela, *J. geophys. Res.,* **112**(B11), doi:10.1029/2006JB004802.

Pan, S. & Niu, F., 2011. Large contrasts in crustal structure and composition between the Ordos plateau and the NE Tibetan plateau from receiver function analysis, *Earth planet. Sci. Lett.,* **303,** 291–298.

Peng, X. & Humphreys, E.D., 1997. Moho dip and crustal anisotropy in northwestern Nevada from teleseismic receiver functions, *Bull. seism. Soc. Am.,* **87,** 745–754.

Savage, M.K., 1998. Lower crustal anisotropy or dipping boundaries?Effects on receiver functions and a case study in New Zealand, *J. geophys. Res.,* **103,** 15 069–15 087.

Shiomi, K. & Park, J., 2008. Structural features of the subducting slab beneath the Kii Peninsula, central Japan: seismic evidence of slab segmentation, dehydration, and anisotropy, *J. geophys. Res.,* **113**(B10), doi:10.1029/2007JB005535.

Silver, P.G., 1996. Seismic anisotropy beneath the continents: probing the depth of geology. Annu. Rev. *Earth planet. Sci.,* **24**(1), 385–432.

Sun, Y. & Toksoz, M.N., 2006. Crustal structure of China and surrounding regions from *P* wave traveltime tomography, *J. geophys. Res.,* **111,** doi:10.1029/2005JB003962.

Sun, Y., Niu, F., Liu, H., Chen, Y. & Liu, J., 2012. Crustal structure and deformation of the SE Tibetan plateau revealed by receiver function data, *Earth planet. Sci. Lett.,* **349,** 186–197.

Tapponnier, P., Xu, Z.Q., Francoise, R., Bertrand, M., Nicolas, A., Gerard, W. & Yang, J.S., 2001. Oblique stepwise rise and growth of the Tibet Plateau, *Science,* **294,** 1671–1677.

Tarkov, A.P. & Vavakin, V.V., 1982. Poisson's ratio behavior in various crystalline rocks: application to the study of the Earth's interior, *Phys. Earth planet. Int.,* **29,** 24–29.

Vinnik, L.P., 1977. Detection of waves converted from P to SV in the mantle, *Phys. Earth planet. Int.,* **15,** 39–45.

Wang, C.Y., Chan, W.W. & Mooney, W.D., 2003. Three-dimensional velocity structure of crust and upper mantle insouthwestern China and its tectonic implications, *J. geophys. Res.,* **108,** 2442, doi:10.1029/2002JB001973, 2003.

Wang, Q. & Gao, Y., 2014. Rayleigh wave phase velocity tomography and strong earthquake activity on the southeastern front of the Tibetan plateau, *Sci. China Earth Sci.,* **57,** 2532–2542.

Wang, Q., Gao, Y., Shi, Y.T. & Wu, J, 2013. Seismic anisotropy in the uppermost mantle beneath the northeastern margin of Qinghai-Tibet plateau: evidence from shear wave splitting of SKS, PKS and SKKS, *Chinese J. Geophys. (in Chinese).,* **56,** 892–905.

Watanabe, T., 1993. Effects of water and melt on seismic velocities and their application to characterization of seismic reflectors, *Geophys. Res. Lett.,* **20,** 2933–2936.

Watson, M.P., Hayward, A.B., Parkinson, D.N. & Zhang, Z.M., 1987. Plate tectonic history, basin development and petroleum source rock deposition onshore China, *Mar. Petrol. Geol.,* **4,** 205–225.

Yang, Y.J., Ritzwoller, M.H., Zheng, Y., Shen, W.S., Levshin, A. & Xie, Z., J., 2012. A synoptic view of the distribution and connectivity of the mid-crustal low velocity zone beneath Tibet, *J. geophys. Res.,* **117**(B04303), doi:10.1029/2011JB008810.

Yao, H., Van der Hilst, R.D. & Montagner, J.P., 2010. Heterogeneity and anisotropy of the lithosphere of SE Tibet from surface wave array tomography, *J. geophys. Res.,* **115,** B12307, doi:10.1029/2009JB007142.

Yin, A. & Harrison, T.M., 2000. Geologic evolution of the Himalayan-Tibetan orogen, *Annu. Rev. Earth planet. Sci.,* **28,** 211–280.

Zandt, G. & Ammon, C., 1995. Continental crust composition constrained by measurements of crustal Poisson's ratio, *Nature,* **374,** 152–154.

Zhang, H., Gao, Y., Shi, Y.T., Liu, X.F. & Wang, Z.X., 2012. Tectonic stress analysis based on the crustal seismic anisotropy in the northeastern margin of Tibetan plateau, *Chinese J. Geophys. (in Chinese),* **55,** 95–104.

Zhang, P.Z. *et al.* 2004. Continuous deformation of the Tibetan plateau from global positioning system data, *Geology,* **32,** 809–812.

Zhang, S.Q. & Karato, S., 1995. Lattice preferred orientation of olivine aggregates deformed in simple shear, *Nature,* **375,** 774–777.

Zhu, L.P. & Helmberger, D.V., 1998. Moho offset across thenorthern margin of the Tibetan plateau, *Science,* **281,** 1170–1172.

Zhu, L.P. & Kanamori, H., 2000, Moho depth variation in southern California from teleseismic receiver functions, *J. geophys. Res.,* **105,** 2969–2980.

SUPPORTING INFORMATION

Additional Supporting Information may be found in the online version of this paper:

Table S1. Measured Moho depth, V_P/V_S ratio and azimuthal anisotropy.

Figure S1. The H–κ analysis results of all the 171 stations that are listed in the table S1, plotted similarly to Fig. 3(a).

Figure S2. The results of the Moho depth (top) and *Vp*/*Vs* ratio (below) obtained at all the stations with their names being marked for better reviewing. (http://gji.oxfordjournals.org/lookup/suppl/doi:10.1093/gji/ggv420/-/DC1).

Please note: Oxford University Press is not responsible for the content or functionality of any supporting materials supplied by the authors. Any queries (other than missing material) should be directed to the corresponding author for the paper.